

# Multi-Resolution Spatio-Temporal Prediction with Application to Wind Power Generation

Shixiang Zhu, Hanyu Zhang, Yao Xie, Pascal Van Hentenryck

**Abstract**—This paper proposes a spatio-temporal model for wind speed prediction which can be run at different resolutions. The model assumes that the wind prediction of a cluster is correlated to its upstream influences in recent history, and the correlation between clusters is represented by a directed dynamic graph. A Bayesian approach is also described in which prior beliefs about the predictive errors at different data resolutions are represented in a form of Gaussian processes. The joint framework enhances the predictive performance by combining results from predictions at different data resolution and provides reasonable uncertainty quantification. The model is evaluated on actual wind data from the Midwest U.S. and shows a superior performance compared to traditional baselines.

**Index Terms**—spatio-temporal model, wind speed prediction, multi-resolution model.

## I. INTRODUCTION

The share of wind in the energy mix, and the number of wind energy installations, continue to grow and will be a key component of a significantly greener grid in the decades to come [1]. Moreover, according to the U.S. Department of Energy (DOE), [2], wind energy is predicted to surpass other sources of renewable power generation within this decade. Wind energy sources, however, suffer from inherent variability and limited predictability and have led to a significant increase in forecasting errors for some Independent System Operators (ISOs), introducing additional challenges for the market-clearing algorithms, which are the backbone of grid operations. As a result, there is a strong need for novel forecasting methods that can *quantify* and *reduce* the uncertainty of wind power predictions and enable grid operators to act effectively [3].

One possible way to manage the increased uncertainty of wind energy sources is to reduce the prediction resolution by clustering wind farms according to their proximity or estimating average wind conditions over a more extended period. Such spatial or temporal aggregations of wind data can not only lower the uncertainty and make the wind energy more predictable but also significantly reduce the scale of the problem, simplify

TABLE I: Comparison of wind speed predictions at different data resolutions. Predictions in some resolution may demonstrate better performance than others under certain circumstances.

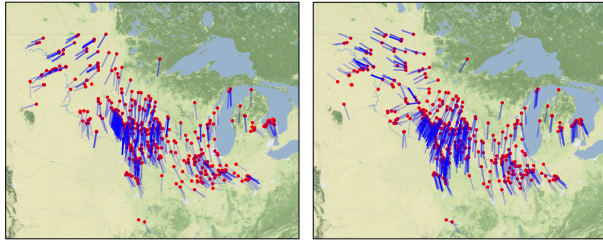
	High space resolution	Low space resolution	High time resolution	Low time resolution
Data Granularity	High	Low	High	Low
Computational Efficiency	Low	High	Low	High
Predictive Uncertainty	High	Low	Low	High
Predictive Accuracy	Low	High	High	Low

the training of the forecasting algorithms, and make the downstream market-clearing algorithms more tractable. However, over-simplifications of the spatio-temporal relationships between wind farms may result in a significant loss of information related to wind direction and speed. In particular, recent upstream wind conditions play a pivotal role in predicting future downstream wind power generation. As shown in Table I, the tradeoff between wind predictions in high and low data resolutions crave more powerful models that may consider complex spatio-temporal dependencies between clusters while leveraging results from predictions at different data resolutions.

This paper first presents a spatio-temporal delayed regressive model for wind speed prediction under specified data resolutions; the wind speed can then be transformed to power generation by a non-linear mapping [4], [5]. The wind direction at each cluster is encoded by a directed dynamic (time-varying) graph, where a directed edge gives the direction of wind blowing from one cluster to the other. To consider the physical propagation delay as the wind must travel from upstream to downstream, the model includes a carefully crafted kernel function that captures the delayed triggering effects between clusters. The model can be efficiently estimated by minimizing an adaptive mean square prediction error.

The paper then develops a multi-resolution model for data at different time and spatial scales and captures the correlated multi-resolution predictions using the Gaussian process. We consider a separable kernel for the Gaussian process to capture the covariance of prediction errors at different spatio-temporal coordinates and different data resolutions. To tackle the computational challenge of the Gaussian process with a large-scale data set, we leverage sparsity in the model, which enables efficient model fitting via a variational learning strategy. Numerical

S. Zhu, H. Zhang, Y. Xie, P. Van Hentenryck were with H. Milton Stewart School of Industrial and Systems Engineering, Georgia Institute of Technology, Atlanta, GA, 30332 USA e-mail: shixiang.zhu@gatech.edu.



(a) 12:00 AM, Sept 21, 2020 (b) 12:00 PM, Sept 21, 2020

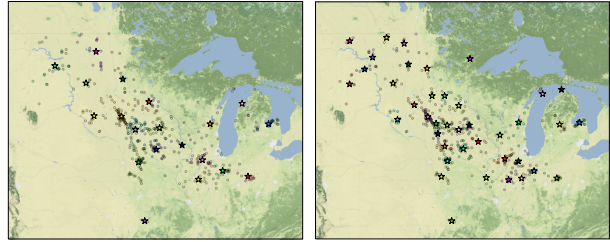
Fig. 1: Examples of the real wind data: 506 wind farms in the Midwestern United States, where the red dots indicate the location of these farms. The blue lines indicate the wind directions and the line widths represent the wind speeds. Coordinates have been shifted to maintain confidentiality.

results show that the good predictive performance of the proposed model. Moreover, we demonstrate that the multi-resolution model can significantly reduce forecasting errors while providing reasonable uncertainty quantification.

The remainder of this paper is organized as follows. After discussing related work, Section II describes the data sets and preliminary analysis. Section III presents the spatio-temporal delayed regressive model. Section IV introduces the multi-resolution spatio-temporal Kriging model and its variational learning strategy. Lastly, Section V presents the numerical results.

*Related work.* There has been an extensive research effort devoted to wind prediction (e.g., [6]–[8]). Early attempts [9]–[11] resort to physical models, relying on parameterizations based on a detailed physical description of the atmosphere. For instance, the Numeric Weather Prediction (NWP) usually runs 1 or 2 times per day due to the difficulty and cost of acquiring real-time information, which limits its usefulness to medium to long-term forecasts (> 6 hours ahead) [6], [7]. Kosovic et al [12] mentions that “the best strategies for nowcasts (0- to about 3-hour ahead) rely on observations near the wind farm”. Many statistical methods [13]–[19] predict the wind speed or power using past observations and time series models, e.g., an autoregressive model (AR). These models are simple and provide timely and reasonably accurate predictions. Recent work has focused on machine-learning models for wind prediction [20], [21]. In particular, recurrent neural networks have been widely adopted to model wind time series and make predictions sequentially [22]–[25]. However, most of the above methods fail to provide uncertainty quantification about their predictions and do not consider spatio-temporal correlations between observations or assume that spatial correlations are time-invariant.

A few studies investigated the uncertainty quantification of wind power forecasts [26]–[28]. However, most of these approaches assume that the distribution of wind speed/power is in a parametric form and do not consider



(a)  $\kappa = 20$  (b)  $\kappa = 40$

Fig. 2: Spatial map of the wind farm groups (stars). Farms (dots) are grouped according to their proximity using the  $k$ -means algorithm. The farms in the same group have the same color.

correlations between different data resolutions. The multi-resolution framework proposed in this paper is related to multi-fidelity models [29], which provide predictive confidence intervals by capturing the correlation between different fidelity levels through a Kriging model. The main difference is that this paper jointly models correlations across time, space, and data resolution.

## II. DATA OVERVIEW AND PRELIMINARY ANALYSIS

The data in this study include 506 wind farms operated or planned by the Midcontinent Independent System Operator (MISO), which delivers safe, cost-effective electric power to 42 million customers across 15 U.S. states and the Canadian province of Manitoba. MISO’s grid includes 71,800 miles of transmission lines and a generation capacity of 177,760 MW for a peak summer system demand of 127,125 MW. We collected eight days of location-specific quarter-hourly *wind speed* and *wind direction* values, starting from September 2020, for each of these wind farms. The wind speed is reported in meters per second (m/s), and the wind direction is reported in cardinal (or compass) directions (in degrees) from which it originates. Fig. 1 presents the spatial map of the wind farms and the wind data at two specific times.

The wind data were prepared at different time and space resolutions. Denote by  $K = 506$  the total number of wind farms in the region of interest and by  $T = 750$  the total number of time units (15 minutes per unit) in the time horizon. Let  $\kappa \in \{1, 2, \dots, K\}$  be the space resolution (the number of clusters) and  $\eta \in \{1, 2, \dots, T\}$  be the time resolution (the number of time units). For the space domain, wind farms can be partitioned into  $\kappa$  clusters using the  $k$ -means algorithm based on their Euclidean distances, with each wind farm belonging to the cluster with the nearest centroid (Fig. 2). Each cluster is indexed by  $i$  with its centroid’s latitude and longitude  $s_i^\kappa \in \mathcal{S} \subset \mathbb{R}^2$ , where  $\mathcal{S}$  represents the space of geographic coordinate system (GCS). For the time domain, the time horizon can be evenly divided into  $T/\eta$  frames, indexed by  $t$  (Fig. 3). Given a data resolution  $(\kappa, \eta)$ , the wind

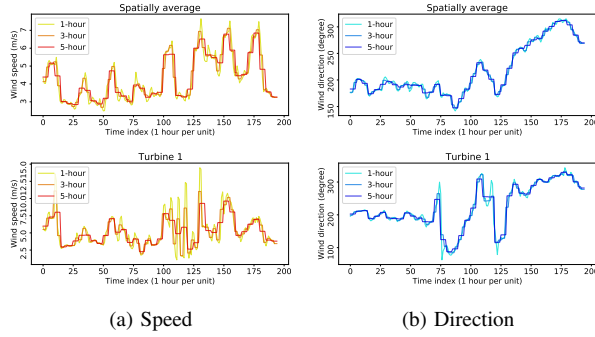


Fig. 3: Examples of (a) wind speed and (b) wind direction in three time resolutions:  $\eta = 4$  (1-hour),  $\eta = 12$  (3-hour), and  $\eta = 20$  (5-hour).

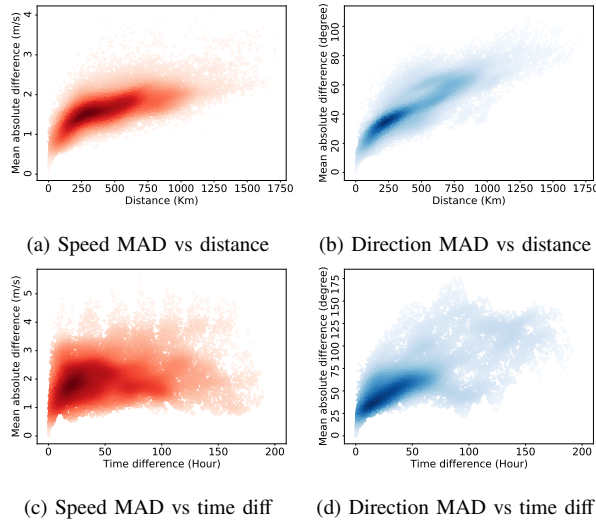


Fig. 4: Data similarity versus distance and time differences. The top panels show the mean absolute difference of (a) the wind speed (m/s) and (b) the wind direction (degree) between two arbitrary locations versus their distance, respectively. The bottom panels show the mean absolute difference of (c) the wind speed (m/s) and (d) the wind direction (degree) of the same location between two time points. The color depth indicates the density of these points; the darker the denser.

speed and direction are averaged for each of the  $\kappa$  clusters and every  $\eta$  time unit.

A preliminary analysis suggests that the wind data exhibit clear dependencies across time and space. This is illustrated in Fig. 4. Fig. 3 also highlights that the wind speed changes more frequently than the wind direction, suggesting that the variation of wind speed in this study is highly dynamic.

### III. SPATIO-TEMPORAL DELAYED REGRESSIVE MODEL

Consider the average wind speed and wind direction of a set of clusters  $\mathcal{V}^\kappa = \{i : 1 \leq i \leq \kappa\}$  at time points  $\mathcal{T}^\eta = \{t : 1 \leq t \leq T/\eta\}$  under data resolution  $(\kappa, \eta)$ . The wind speed for cluster  $i$  at time  $t$  is assumed to be correlated with the historic wind speed at the upstream

wind farms before time  $t$ . The wind directions, from cluster to cluster, can be specified by a directed *dynamic* graph  $\mathcal{G}^{\kappa, \eta} = (\mathcal{V}^\kappa, \{\mathcal{E}_t^\kappa\}_{t \in \mathcal{T}^\eta})$ , where  $\mathcal{V}^\kappa$  represents the clusters,  $\mathcal{E}_t^\kappa \subseteq \mathcal{E}^\kappa$  is a set of directed edges (ordered pairs of vertices) connecting two clusters if the wind blows from the source cluster to the target cluster at time  $t$ , and  $\mathcal{E}^\kappa$  denotes the fully-connected graph with  $\kappa$  vertices.

Let  $y_{it}^{\kappa, \eta}$  be the true average wind speed of cluster  $i$  at time  $t$  under data resolution  $(\kappa, \eta)$  and let  $f^{\kappa, \eta}(i, t)$  be the corresponding wind speed prediction. The spatio-temporal delayed regressive model for the wind speed prediction is specified by:

$$f^{\kappa, \eta}(i, t) = \mu_i^\kappa + \sum_{\tau=t-d}^{t-1} \sum_{j:(j,i) \in \mathcal{E}_\tau^\kappa} g^{\kappa, \eta}(t, \tau, i, j), \quad (1)$$

$$i \in \mathcal{V}^\kappa, t \in \mathcal{T}^\eta,$$

where  $\mu_i^\kappa$  is a learnable scalar representing the background wind speed in cluster  $i$ ,  $d$  is the chosen memory depth,  $g^{\kappa, \eta}(t, \tau, i, j)$  is a triggering function that describes the “influence” of strong wind energy (m/s) at cluster  $j$  at time  $\tau$  triggers a strong wind energy at cluster  $i$  at time  $t$  (the model is motivated by the Hawkes processes [30] although here we do not consider point processes).

The choice of the triggering function  $g^{\kappa, \eta}$  relies on three key assumptions. (i) The upstream influence decays over time and hence the triggering function includes an exponential function  $\beta \exp\{-\beta(t - \tau)\}$  commonly used to represent such decay, where  $t > \tau \geq 0$  and the parameter  $\beta \geq 0$  captures the decay rate of the influence (note that the function integrates to one over  $t$ ). (ii) The inter-cluster influence varies from pair to pair and may depend on the geographical features of the region that lie between two clusters. Hence each edge  $(j, i) \in \mathcal{E}$  is associated with a non-negative weight  $\alpha_{ji}^{\kappa, \eta} \geq 0$  indicating the correlation between cluster  $i$  and  $j$ : the larger the weight  $\alpha_{ji}^{\kappa, \eta}$ , the cluster  $i$  is more likely to be affected by cluster  $j$ . (iii) The upstream influence has a physical propagation delay as the wind must travel over the Earth’s surface to reach the downstream cluster [31]; such delay can be estimated by the distance between two clusters divided by the wind speed at that time. In summary, the triggering function can be expressed as

$$g^{\kappa, \eta}(t, \tau, i, j) = \alpha_{ji}^{\kappa, \eta} \beta_j^{\kappa, \eta} \exp\{-\beta_j^{\kappa, \eta}(t - \tau - \lambda_{ji\tau}^{\kappa, \eta})\} \cdot y_{j\tau}^{\kappa, \eta} \cdot \mathbb{1}\{t - \tau \geq \lambda_{ji\tau}^{\kappa, \eta}\},$$

$$i, j \in \mathcal{V}^\kappa, t, \tau \in \mathcal{T}^\eta,$$

where  $\{\lambda_{ji\tau}^{\kappa, \eta} > 0\}$  is a tensor of wind travel times (in seconds) from cluster  $j$  to cluster  $i$  at time  $t$  estimated from real data and  $\beta_j^{\kappa, \eta} \geq 0$  is the decay rate of cluster  $j$ ’s influence. Since the model assumes that  $\alpha_{ii}^{\kappa, \eta} = 1$ ,  $i \in \mathcal{V}^\kappa$ ,  $\beta_j^{\kappa, \eta}$  can be regarded as the influence’s decay rate of cluster  $j$ .

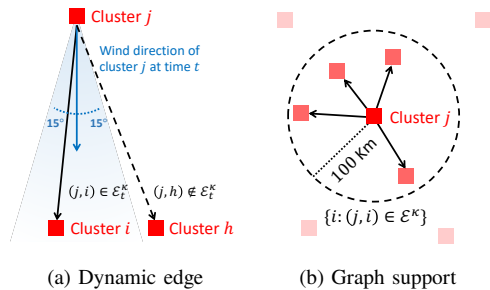


Fig. 5: Illustrations of (a) an edge in the DDG and (b) the support of DDG for one of the clusters.

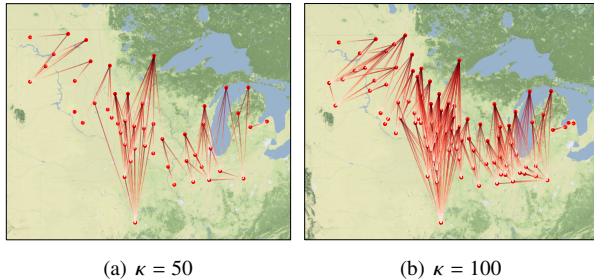


Fig. 6: Examples of DDGs for wind direction with different space resolutions. The lines represent the wind direction from one cluster to another, where the dark red end indicates the upstream cluster and the light red end the downstream cluster.

*Directed dynamic graph for wind direction.* The directed dynamic graph (DDG)  $\mathcal{G}^{\kappa, \eta}$  in (1) defines the wind direction between clusters, which can be extracted from the raw data. Given a data resolution  $(\kappa, \eta)$ , the dynamic graph includes the directed edge from cluster  $j$  to  $i$  at time  $t$  if the difference between their wind directions at that time is not larger than  $15^\circ$ , as illustrated in Fig. 5 (a). Appendix A gives the algorithm for extracting the DDG. The graph support  $\mathcal{E}^\kappa$  has a sparse structure: indeed, the preliminary analysis in Section II indicates that an arbitrary cluster can only be affected by its nearest clusters within a 100-Km radius of itself, as shown in Fig. 5 (b). The sparsity of the graph support leads to significant reductions in the calculation of (1) and plays a big role in the computational efficiency of the proposed model. Fig. 6 presents two examples of extracted DDG using the real wind data in different space resolutions.

*Model estimation.* The model with resolution  $(\kappa, \eta)$  can be estimated by minimizing the mean square error between the true wind speed and its prediction. Denote the set of the parameters of the model  $f^{\kappa, \eta}$  as  $\theta^{\kappa, \eta} := \{\{\mu_i^\kappa\}, \{\alpha_{ij}^{\kappa, \eta}\}, \{\beta_i^{\kappa, \eta}\}\} \in \Theta^\kappa$ , where  $\Theta^\kappa \subseteq \mathbb{R}_+^\kappa \times \mathbb{R}_+^{\kappa \times \kappa} \times \mathbb{R}_+^\kappa$  is the corresponding parameter space. It is noteworthy that the model includes less than  $\kappa(2 + \kappa)$  parameters thanks to the sparse structure of  $\{\alpha_{ij}^{\kappa, \eta}\}$ . The model can be effectively learned by using  $\kappa(T/\eta)$  points under resolution  $(\kappa, \eta)$ , where  $\kappa \ll T/\eta$ ; for example,

when  $\kappa = 20, \eta = 4$ , there are about 120 parameters and 3,740 data points. The over-prediction of future wind power may result in fewer commitments of other types of generators, creating reliability issues. To this end, the loss function for training the model includes a scaling factor that penalizes overestimations. Formally, the optimal parameters can be found by solving the following optimization problem:

$$\arg \min_{\theta^{\kappa, \eta} \in \Theta^{\kappa, \eta}} l(\theta^{\kappa, \eta}) := \sum_{t=1}^{T/\eta} \sum_{i=1}^{\kappa} \left( e_{it}^{\kappa, \eta} + \delta \mathbb{1} \{y_{it}^{\kappa, \eta} \leq f^{\kappa, \eta}(i, t)\} e_{it}^{\kappa, \eta} \right),$$

where  $e_{it}^{\kappa, \eta} := [y_{it}^{\kappa, \eta} - f^{\kappa, \eta}(i, t)]^2$  denotes the square error of the prediction and  $\delta \geq 0$  is a factor that controls the magnitude of penalization for the overestimation.

#### IV. MULTI-RESOLUTION SPATIO-TEMPORAL KRIGING

Multi-resolution modeling enables the seamless fusion of information from a collection of heterogeneous sources of predictions with various accuracies and uncertainties. These predictions can be considered correlated “experts”, and each of them may outperform others under certain circumstances (see Table I). By capturing the cross-correlation between these sources, one can construct surrogate models that can dramatically improve the predictive performance. These deterministic estimators at different data resolutions also enjoy a degree of smoothness, in the sense that the output values for similar spatio-temporal coordinates are reasonably close.

This section presents a new method to correct the deterministic prediction results by adding a noise term, that captures the prior belief about each level of the predictions via a Kriging model. Consider the real wind speeds  $\{y_{it}^{\kappa, \eta}\}$  and their deterministic predictions  $\{f^{\kappa, \eta}(i, t)\}$  using the method described in Section III under different data resolutions  $(\kappa, \eta) \in \mathcal{R}$ , where  $\mathcal{R}$  denotes the set of data resolutions. The goal is to find a corrected estimator that improves the predictive accuracy and reduces uncertainty by leveraging the information across different data sets with different resolutions. The proposed multi-resolution Kriging model is given by

$$y_{it}^{\kappa, \eta} = f^{\kappa, \eta}(i, t) + \epsilon(i, t, \kappa, \eta) + c_i^\kappa, \quad i \in \mathcal{V}^\kappa, t \in \mathcal{T}^\eta, \quad (2)$$

where  $\epsilon(i, t, \kappa, \eta)$  denotes the error of the deterministic estimator and follows a zero-mean Gaussian process whose covariance is specified by a kernel function  $k$ . We also introduce a constant  $c_i^\kappa > 0$  representing the mean prediction error for each cluster if the overestimations are penalized ( $\delta > 0$ ), which can be estimated empirically by averaging the prediction errors of cluster  $i$ , i.e.,  $(\sum_{t=1}^{T/\eta} (y_{it}^{\kappa, \eta} - f^{\kappa, \eta}(i, t))^2) / (T/\eta)$ .

For simplicity, denote the spatio-temporal coordinate of a cluster  $i$  at time  $t$  under data resolution  $(\kappa, \eta)$  by  $\mathbf{x} := (i, t, \kappa, \eta) \in \mathcal{X}$ , where  $\mathcal{X}$  represents the corresponding joint space. For any subset  $\mathbf{X} \subseteq \mathcal{X}$  with  $N$  coordinates, the corresponding real wind speeds and their predictions are denoted by  $\mathbf{y} := \{y_{it}^{\kappa, \eta}\}$  and  $\mathbf{f} := \{f^{\kappa, \eta}(i, t)\}$ , respectively. Assume that the set of function variables  $\boldsymbol{\epsilon} := \{\epsilon(i, t, \kappa, \eta)\}$  has joint (zero-mean) distribution

$$p(\boldsymbol{\epsilon}) = \mathcal{N}(\boldsymbol{\epsilon} \mid \mathbf{0}, \mathbf{K}_{XX}), \quad (3)$$

where  $\mathbf{K}_{XX}$  is an  $N \times N$  matrix and its entries are pairwise evaluations of  $k(\mathbf{x}, \mathbf{x}')$ ,  $\forall \mathbf{x}, \mathbf{x}' \in \mathbf{X}$ . Here  $\mathcal{N}(x \mid \boldsymbol{\mu}, \boldsymbol{\Sigma})$  is the probability density function of variable  $x$  that follows a Gaussian distribution with mean  $\boldsymbol{\mu}$  and variance  $\boldsymbol{\Sigma}$ . The conditional probability of  $\mathbf{y}$  can then be expressed as

$$p(\mathbf{y}) = \mathcal{N}(\mathbf{y} \mid \mathbf{f}, \mathbf{K}_{XX}), \quad (4)$$

The parameters of the Kriging model are optimized by maximizing the log marginal likelihood of wind speeds:

$$\begin{aligned} \arg \max_{\sigma \in \Sigma} \ell(\sigma) &:= \log p(\mathbf{y}) = \\ &= -\frac{1}{2} (\mathbf{y} - \mathbf{f})^\top \mathbf{K}_{XX}^{-1} (\mathbf{y} - \mathbf{f}) - \frac{1}{2} \log |\mathbf{K}_{XX}| - \frac{N}{2} \log 2\pi, \end{aligned} \quad (5)$$

where  $\sigma$  denotes the set of model parameters and  $\Sigma$  is the corresponding parameter space; the Gram matrix  $\mathbf{K}_{XX}$  is invertible because, in practice, the time and space of data points are not linearly dependent.

#### A. Kernel design for time, space, and data resolution

This section discusses the choice of the kernel function  $k$ . Standard GP models use a stationary covariance, in which the covariance between any two points is a function of Euclidean distance. In this study, the kernel requires a difference covariance structure, since it contains both spatio-temporal coordinates and data resolution. The kernel design first assumes that the time, space, and data resolution are mutually independent, as each of these factors describes the wind power in a different domain. The correlation function is thus separable, i.e.,

$$\begin{aligned} k((i, t, \kappa, \eta), (j, \tau, \kappa', \eta')) &= \\ \nu_s(i, \kappa, j, \kappa') \cdot \nu_t(t, \eta, \tau, \eta') \cdot \nu_s(\kappa, \kappa') \cdot \nu_t(\eta, \eta'), \\ i &\in \mathcal{V}^\kappa, j \in \mathcal{V}^{\kappa'}, t \in \mathcal{T}^\eta, \tau \in \mathcal{T}^{\eta'}. \end{aligned}$$

The temporal and spatial kernels are also assumed to be commonly-used Gaussian correlation functions:

$$\begin{aligned} \nu_s(i, \kappa, j, \kappa') &= \exp \left\{ -\sigma_s \|s_i^\kappa - s_j^{\kappa'}\|^2 \right\}, \quad i \in \mathcal{V}^\kappa, j \in \mathcal{V}^{\kappa'}, \\ \nu_t(t, \eta, \tau, \eta') &= \exp \left\{ -\sigma_t (t\eta - \tau\eta')^2 \right\}, \quad t \in \mathcal{T}^\eta, \tau \in \mathcal{T}^{\eta'}, \end{aligned}$$

where  $\sigma_s > 0$  and  $\sigma_t > 0$  are two learnable parameters. Recall that  $s_i^\kappa$  represents the geographical location of the

cluster  $i$  and  $t\eta$  is the recorded time (*not* the time index) under the data resolution  $(\kappa, \eta)$ .

Designation of  $\nu_s$  and  $\nu_t$  requires more deliberation. According to Fig. 7, they cannot be zero when  $\kappa = \kappa'$  or  $\eta = \eta'$  and would become larger as  $\kappa$  or  $\eta$  increases. Therefore, the following correlation function for both  $\nu_s$  and  $\nu_t$  was selected:

$$\begin{aligned} \nu_s(\kappa, \kappa') &= \exp \left\{ -\sigma_0^\kappa (\kappa - \kappa')^2 \right\} + \\ &\quad \exp \left\{ -\sigma_1^\kappa (\kappa - K)^2 \right\} + \exp \left\{ -\sigma_1^\kappa (\kappa' - K)^2 \right\}, \\ \nu_t(\eta, \eta') &= \exp \left\{ -\sigma_0^\eta (\eta - \eta')^2 \right\} + \\ &\quad \exp \left\{ -\sigma_1^\eta (\eta - T)^2 \right\} + \exp \left\{ -\sigma_1^\eta (\eta' - T)^2 \right\}, \end{aligned}$$

where  $\sigma_0^\kappa > 0$ ,  $\sigma_1^\kappa > 0$ ,  $\sigma_0^\eta > 0$ , and  $\sigma_1^\eta > 0$  are learnable parameters.

#### B. Variational learning for large-scale data set

The GP approach is notoriously intractable for large datasets since the computations require the inversion of a matrix of size  $N \times N$  which scales as  $O(N^3)$  [32]. In this study, the data set includes 11 different data resolutions, with up to 190 time indices and 50 clusters, resulting in  $N \approx 95,000$ . To address the tractability issues, this paper derives sparse models for the noise  $\boldsymbol{\epsilon}$  inspired by [33]–[36]. The idea is to introduce a small set of  $M$  auxiliary inducing variables  $\mathbf{u}$  evaluated at the pseudo-inputs  $\mathbf{Z} := \{z \in \mathcal{X}\}$  that aim to best approximate the training data. The initial inputs  $\mathbf{Z}$  are a subset of spatio-temporal coordinates that are randomly sampled from the training inputs [37]. It is then possible to adopt a variational learning strategy for such a sparse approximation and jointly infer the optimal inducing inputs and other model parameters by maximizing a lower bound of the true log marginal likelihood.

Inducing variables  $\mathbf{u}$  are function points drawn from the same GP prior as the training functions  $\boldsymbol{\epsilon}$  in (3), so the joint distribution can be written as

$$p(\boldsymbol{\epsilon}, \mathbf{u}) = \mathcal{N} \left( \begin{bmatrix} \boldsymbol{\epsilon} \\ \mathbf{u} \end{bmatrix} \mid \mathbf{0}, \begin{bmatrix} \mathbf{K}_{XX} & \mathbf{K}_{XZ} \\ \mathbf{K}_{XZ}^\top & \mathbf{K}_{ZZ} \end{bmatrix} \right), \quad (6)$$

where  $\mathbf{K}_{ZZ}$  is formed by evaluating the kernel function pairwise at all pairs of inducing points in  $\mathbf{Z}$ , and  $\mathbf{K}_{XZ}$  is formed by evaluating the kernel function across the data points  $\mathbf{X}$  and inducing points  $\mathbf{Z}$  similarly.

To obtain a computationally efficient inference, the posterior distribution  $p(\boldsymbol{\epsilon}, \mathbf{u} \mid \mathbf{y})$  over random variable vector  $\boldsymbol{\epsilon}$  and  $\mathbf{u}$  is approximated by a variational distribution  $q(\boldsymbol{\epsilon}, \mathbf{u})$ . Assume that this variational distribution  $q(\boldsymbol{\epsilon}, \mathbf{u})$  can be factorized as  $q(\boldsymbol{\epsilon}, \mathbf{u}) := p(\boldsymbol{\epsilon} \mid \mathbf{u})q(\mathbf{u})$ . To jointly determine the variational parameters and model parameters  $\sigma = \{\sigma_s, \sigma_t, \{\sigma_0^\kappa, \sigma_1^\kappa\}, \{\sigma_0^\eta, \sigma_1^\eta\}\}$ , the variational evidence lower bound (ELBO) [38] substitutes for the marginal likelihood  $\ell(\sigma)$  defined in (5):

$$\log p(\mathbf{y}) \geq \mathbb{E}_{q(\boldsymbol{\epsilon})} [\log p(\mathbf{y} \mid \boldsymbol{\epsilon})] - \text{KL} [q(\mathbf{u}) \parallel p(\mathbf{u})], \quad (7)$$



where  $\text{KL}[q||p]$  denotes the Kullback–Leibler (KL) divergence between two distributions  $q$  and  $p$  [39]. The derivation defines  $q(\boldsymbol{\epsilon}) := \int p(\boldsymbol{\epsilon}|\mathbf{u})q(\mathbf{u})d\mathbf{u}$  and assumes  $q(\mathbf{u}) := \mathcal{N}(\mathbf{u}|\mathbf{m}, \mathbf{S})$ , which is the most common way to parameterize the prior distribution of inducing variables in terms of a mean vector  $\mathbf{m}$  and a covariance matrix  $\mathbf{S}$ . To ensure that the covariance matrix remains positive definite, it can be represented as a lower triangular form  $\mathbf{S} = \mathbf{L}\mathbf{L}^\top$ . This leads to the analytical form for  $q(\boldsymbol{\epsilon})$ :

$$q(\boldsymbol{\epsilon}) = \mathcal{N}(\boldsymbol{\epsilon} | \mathbf{A}\mathbf{m}, \mathbf{K}_{XX} + \mathbf{A}(\mathbf{S} - \mathbf{K}_{ZZ})\mathbf{A}^\top),$$

where  $\mathbf{A} = \mathbf{K}_{XZ}\mathbf{K}_{ZZ}^{-1}$ . The likelihood can also be factorized as  $p(\mathbf{y}|\boldsymbol{\epsilon}) = \prod_{n=1}^N p(y_n|\epsilon_n)$  for the ease of computation in (7). Therefore, the ELBO objective can be rewritten as

$$\begin{aligned} \ell_{\text{ELBO}}(\sigma, \mathbf{Z}, \mathbf{m}, \mathbf{S}) := \\ \sum_{n=1}^N \mathbb{E}_{q(\epsilon_n)} [\log p(y_n|\epsilon_n)] - \text{KL}[q(\mathbf{u})||p(\mathbf{u})]. \end{aligned} \quad (8)$$

Note that the one dimensional integrals of the log-likelihood in (8) can be computed by Gauss-Hermite quadrature [40] (the derivation of the ELBO can be found in Appendix B). In contrast to directly maximizing the marginal log likelihood defined in (5), computing this objective and its derivatives only costs  $O(NM^2)$ . In practice, the optimization is carried out through stochastic gradient descent (see Appendix C).

### C. Prediction with variational posterior

An one-step ahead prediction for wind speed in cluster  $i$  at time  $t+1$  given the past observations (before time  $t$ ) in resolution  $(\kappa, \eta)$  requires the derivation of the posterior distribution of prediction  $p(\boldsymbol{\epsilon}|\mathbf{y})$ . For all clusters  $i \in \mathcal{V}^\kappa$ , we consider the spatio-temporal coordinates  $\mathbf{X}_t := \{(i, \tau, \kappa, \eta)\}_{\tau \leq t}$ , their observations  $\mathbf{y}_t := \{y_{i\tau}^{\kappa, \eta}\}_{\tau \leq t}$ , and fitted inducing points  $\mathbf{Z}$  and assume that the unobserved future data comes from the same generation process. Therefore, for all the coordinates at the next moment  $\mathbf{X}_* := \{(i, t+1, \kappa, \eta)\}$ , the distribution of one-step-ahead noise prediction  $\boldsymbol{\epsilon}_* := \{\epsilon_*(i, t+1, \kappa, \eta)\}$  is given by

$$p(\boldsymbol{\epsilon}_*|\mathbf{y}_t) = \mathcal{N}(\boldsymbol{\epsilon}_* | \mathbf{A}_*\mathbf{m}, \mathbf{A}_*\mathbf{S}\mathbf{A}_*^\top + \mathbf{B}_*), \quad (9)$$

where  $\mathbf{A}_* = \mathbf{K}_{*Z}\mathbf{K}_{ZZ}^{-1}$  and  $\mathbf{B}_* = \mathbf{K}_{**} - \mathbf{K}_{*Z}\mathbf{K}_{ZZ}^{-1}\mathbf{K}_{*Z}^\top$ . The  $\mathbf{K}_{*Z}$  denotes a  $\kappa \times M$  matrix and its entries are pairwise evaluations of  $k(\mathbf{x}_*, \mathbf{z})$  where  $\mathbf{x}_* \in \mathbf{X}_*$  and  $\mathbf{z} \in \mathbf{Z}$ . The derivation of the predictive posterior can be found in Appendix D. The prediction for the wind speed therefore can be made by plugging (9) into (4).

## V. RESULTS ON THE CASE STUDY

The results consider the wind data at 11 different data resolution as shown in Fig. 10. The proposed spatio-temporal delayed regressive (STDR) model described in

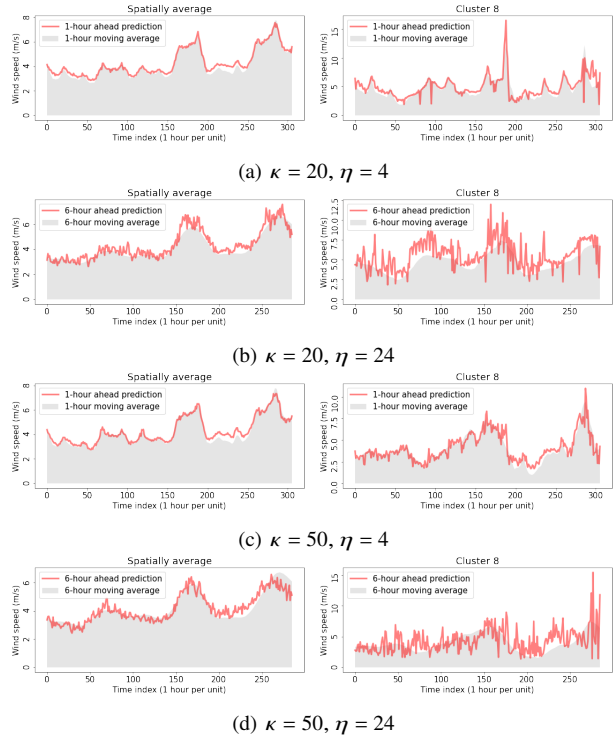


Fig. 7: Examples of prediction using STDR on four data sets with different data resolutions. The 1st column shows the spatially average of prediction and the 2nd column shows the prediction of one of the clusters.

Section III generates deterministic wind speed predictions using for each of these data sets. The predictions are then corrected using the proposed multi-resolution spatio-temporal Kriging (MRSTK) model described in Section IV. The out-of-sample predictive performance of these two approaches is measured using their mean absolute error (MAE). Observe that model MRSTK not only generates accurate predictions, but also quantifies the uncertainty about the predictions. The results report the estimated predictive confidence interval of MRSTK over time and space, respectively. The results are also compared with other baseline approaches. The estimation of each STDR uses Stochastic Gradient Descent (SGD) with a learning rate of  $10^{-2}$  and a scaling factor  $\delta = 0.8$  to penalize the overestimation. The estimated model for predicting wind speed at time  $t$  can be used as the warm start for the model at time  $t+1$ . Model MRSTK with  $M = 500$  inducing variables is estimated with SGD with a learning rate of  $10^{-2}$  and a batch size of 1,000. All experiments are performed on Google Colaboratory (Pro version) with 12GB RAM and dual-core Intel processors, with speeds up to 2.3 GHz (without GPU).

### A. Deterministic spatio-temporal prediction

The STDR's predictive power is assessed by performing the one-step ahead or  $\eta$ -unit ahead (out-of-sample)

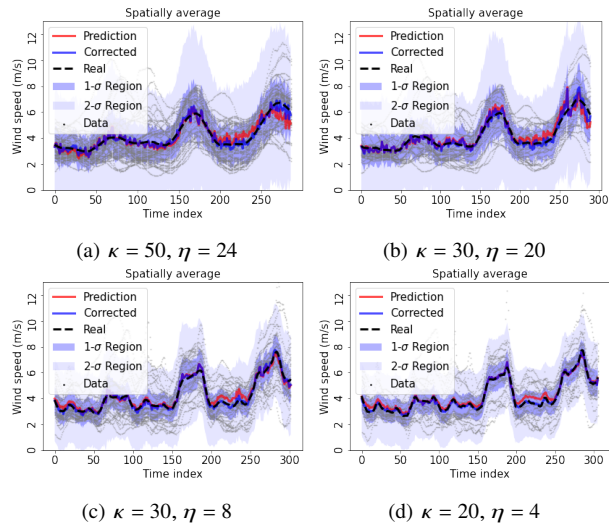


Fig. 8: Examples of corrected prediction suggested by MRSTK on four data sets with different data resolutions. The black dash line and red solid line represent the ground truth and deterministic prediction, respectively. The blue solid line represents the corrected prediction made by MRSTK, where the blue shaded area represents the corresponding confidence interval.

prediction at different data resolutions. The prediction for time index  $t$  given resolution  $(\kappa, \eta)$  is carried out by (i) withholding the data after  $t$  from the model estimation and using the  $\eta$ -unit moving average of historical data before  $t$  to fit the model (Fig. 11 in Appendix F); and (ii) using the fitted model to make predictions for the (hold-out) data at time  $t + 1$ . Fig. 7 presents examples of one-step ahead predictions of STDR at four different data resolutions. Fig. 12 in Appendix F summarize the cluster-wise MAEs for the same four data sets. The above results show that model STDR can predict wind speed accurately at the cluster-level. Observe that high resolution wind speeds oscillate rapidly, with significant amplitude, and increases of data resolution  $(\kappa, \eta)$  will degrade the predictive accuracy significantly. In addition, Fig. 13 and Fig. 14 in Appendix F visualize the fitted  $\{\alpha_{ji}^{\kappa, \eta}\}$  for different  $\kappa$  and their detected community structures using Leiden algorithm [41].

### B. Corrected prediction for multi-resolution data

The learning of model MRSTK uses all the data sets at different resolution and their predictions before time index  $t$  as input in order to correct the prediction of wind speed at the next time step  $t + 1$ . Fig. 8 shows four examples of corrected predictions on four data sets with different resolutions. The blue and red lines indicate the predictions of STDR and MRSTK, respectively. The results show that the MRSTK outperforms the STDR, particularly for the period from 180 to 250. Fig. 8 also presents the estimated confidence interval suggested by MRSTK. The black dots represent the observed wind speeds for

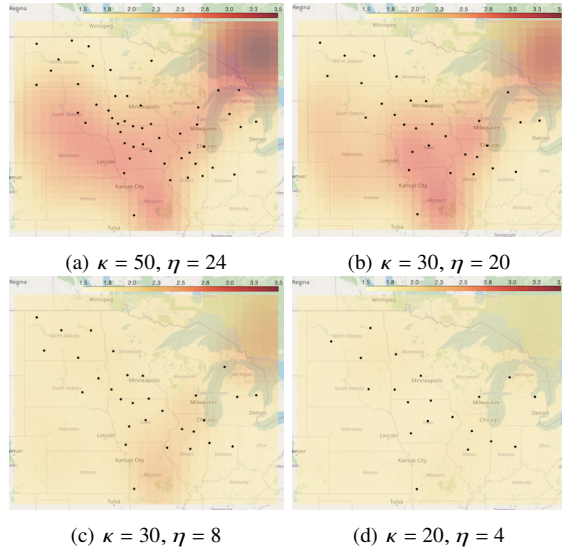


Fig. 9: Examples of the spatial distribution of  $1\sigma$  confidence interval (68.27%) for the corrected prediction suggested by MRSTK on four data sets at different data resolutions. The black dot represents the centroid of cluster; the color depth represents the length of confidence interval (m/s).

TABLE II: Performance comparison of all methods.

	MAE (average)	MAE ( $\kappa = 50, \eta = 24$ )	MAE ( $\kappa = 20, \eta = 4$ )
MRSTK	<b>0.20 (5%)</b>	<b>0.25 (5%)</b>	<b>0.14 (4%)</b>
STDR	0.27 (6%)	0.31 (7%)	0.21 (6%)
NN	0.48 (11%)	0.45 (11%)	0.56 (13%)
LSTM	0.50 (12%)	0.50 (11%)	0.43 (11%)
VAR	0.45 (11%)	0.70 (16%)	0.27 (6%)

a certain cluster; the light and dark shaded blue areas indicate the  $1\sigma$  (68.27%) and  $2\sigma$  (95.45%) prediction intervals, respectively. The result shows that the estimated confidence interval achieves good data coverage. Fig. 9 presents the spatial distribution of the estimated  $1\sigma$  (68.27%) prediction intervals for the same four data sets. The model achieves smaller confidence interval as the data resolution decreases. Note also that the regions with significantly higher predictive uncertainty are where the wind was usually originated. This is due to the fact that the data sets do not have enough upstream observations to infer the wind condition for these regions. Fig. 10 compares the predictive performance between STDR and MRSTK quantitatively on each of the data sets. The results show that the MAEs of MRSTK are significantly lower than those of STDR for all scenarios and confirm the effectiveness of MRSTK.

### C. Comparison with baselines

The proposed models were compared with baseline approaches, including neural network-based uni-variate prediction model (NN), long short-term memory (LSTM),

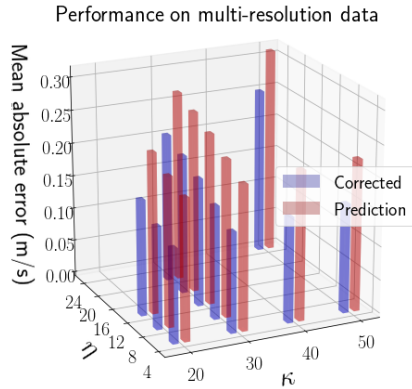


Fig. 10: Performance of our methods on 11 data sets at different data resolutions. The red and blue bar represent the MAE of STDR and MRSTK, respectively.

and vector autoregressive model (VAR); see [6], [7] for detailed review of these predictive algorithms and see Appendix E for their experimental settings and hyperparameter choices. Table II reports the MAE and its percentage with respect to the ground truth for the out-of-sample prediction at cluster-level of the models. They confirm that the proposed models significantly outperform the baseline methods.

## VI. CONCLUSION

This paper proposes a spatio-temporal predictive model for wind speed. A directed dynamic graph is introduced to represent the wind directions between clusters of wind farms. The paper also introduced a Bayesian framework that bridges the gap between data at different resolution through a Gaussian process and significantly enhance the predictive power of the model. The joint framework has shown great promise in modeling and predicting wind speed. The numerical study also showed that the proposed methods have superior predictive performance while providing reasonable uncertainty quantification.

## REFERENCES

- [1] International renewable energy agency, “Wind energy,” <https://www.irena.org/wind>, accessed: 2021-06-12.
- [2] Department of Energy, “Wind vision: A new era for wind power in the united states,” <https://www.energy.gov/eere/wind/maps/wind-vision>, accessed: 2021-06-12.
- [3] P. Pinson *et al.*, “Wind energy: Forecasting challenges for its operational management,” *Statistical Science*, vol. 28, no. 4, pp. 564–585, 2013.
- [4] I. E. Commission *et al.*, “Wind turbines-part 12-1: Power performance measurements of electricity producing wind turbines,” *IEC 61400-12-1*, 2005.
- [5] A. A. Ezzat, M. Jun, and Y. Ding, “Spatio-temporal short-term wind forecast: A calibrated regime-switching method,” *The annals of applied statistics*, vol. 13, no. 3, p. 1484, 2019.
- [6] M. Lei, L. Shiyang, J. Chuanwen, L. Hongling, and Z. Yan, “A review on the forecasting of wind speed and generated power,” *Renewable and Sustainable Energy Reviews*, vol. 13, no. 4, pp. 915–920, 2009. [Online]. Available: <https://www.sciencedirect.com/science/article/pii/S1364032108000282>
- [7] S. S. Soman, H. Zareipour, O. Malik, and P. Mandal, “A review of wind power and wind speed forecasting methods with different time horizons,” in *North American Power Symposium 2010*. IEEE, 2010, pp. 1–8.
- [8] G. Giebel, C. Draxl, R. Brownsword, G. Kariniotakis, and M. Denhard, “The state-of-the-art in short-term prediction of wind power. a literature overview,” 2011.
- [9] C. W. Potter and M. Negnevitsky, “Very short-term wind forecasting for tasmanian power generation,” *IEEE Transactions on power systems*, vol. 21, no. 2, pp. 965–972, 2006.
- [10] M. Lange and U. Focken, “New developments in wind energy forecasting,” in *2008 IEEE power and energy society general meeting-conversion and delivery of electrical energy in the 21st century*. IEEE, 2008, pp. 1–8.
- [11] B. Candy, S. J. English, and S. J. Keogh, “A comparison of the impact of quikscat and windsat wind vector products on met office analyses and forecasts,” *IEEE transactions on geoscience and remote sensing*, vol. 47, no. 6, pp. 1632–1640, 2009.
- [12] B. Kosovic, S. E. Haupt, D. Adriaansen, S. Alessandrini, G. Wiener, L. Delle Monache, Y. Liu, S. Linden, T. Jensen, W. Cheng, M. Politovich, and P. Prestopnik, “A comprehensive wind power forecasting system integrating artificial intelligence and numerical weather prediction,” *Energies*, vol. 13, no. 6, 2020. [Online]. Available: <https://www.mdpi.com/1996-1073/13/6/1372>
- [13] B. G. Brown, R. W. Katz, and A. H. Murphy, “Time series models to simulate and forecast wind speed and wind power,” *Journal of Applied Meteorology and Climatology*, vol. 23, no. 8, pp. 1184–1195, 1984.
- [14] A. Kusiak and W. Li, “Estimation of wind speed: A data-driven approach,” *Journal of Wind Engineering and Industrial Aerodynamics*, vol. 98, no. 10-11, pp. 559–567, 2010.
- [15] E. Erdem and J. Shi, “Arma based approaches for forecasting the tuple of wind speed and direction,” *Applied Energy*, vol. 88, no. 4, pp. 1405–1414, 2011.
- [16] M. He, L. Yang, J. Zhang, and V. Vittal, “A spatio-temporal analysis approach for short-term forecast of wind farm generation,” *IEEE Transactions on Power Systems*, vol. 29, no. 4, pp. 1611–1622, 2014.
- [17] J. Dowell and P. Pinson, “Very-short-term probabilistic wind power forecasts by sparse vector autoregression,” *IEEE Transactions on Smart Grid*, vol. 7, no. 2, pp. 763–770, 2015.
- [18] P. Jiang, S. Qin, J. Wu, and B. Sun, “Time series analysis and forecasting for wind speeds using support vector regression coupled with artificial intelligent algorithms,” *Mathematical Problems in Engineering*, vol. 2015, 2015.
- [19] A. Pourhabib, J. Z. Huang, and Y. Ding, “Short-term wind speed forecast using measurements from multiple turbines in a wind farm,” *Technometrics*, vol. 58, no. 1, pp. 138–147, 2016.
- [20] M. A. Mohandes, T. O. Halawani, S. Rehman, and A. A. Hussain, “Support vector machines for wind speed prediction,” *Renewable energy*, vol. 29, no. 6, pp. 939–947, 2004.
- [21] G. Sideratos and N. D. Hatziaargyriou, “Probabilistic wind power forecasting using radial basis function neural networks,” *IEEE Transactions on Power Systems*, vol. 27, no. 4, pp. 1788–1796, 2012.
- [22] W. Yao, P. Huang, and Z. Jia, “Multidimensional lstm networks to predict wind speed,” in *2018 37th Chinese Control Conference (CCC)*. IEEE, 2018, pp. 7493–7497.
- [23] Y. Liu, L. Guan, C. Hou, H. Han, Z. Liu, Y. Sun, and M. Zheng, “Wind power short-term prediction based on lstm and discrete wavelet transform,” *Applied Sciences*, vol. 9, no. 6, p. 1108, 2019.
- [24] R. Yu, J. Gao, M. Yu, W. Lu, T. Xu, M. Zhao, J. Zhang, R. Zhang, and Z. Zhang, “Lstm-efg for wind power forecasting based on sequential correlation features,” *Future Generation Computer Systems*, vol. 93, pp. 33–42, 2019.
- [25] B. Liu, S. Zhao, X. Yu, L. Zhang, and Q. Wang, “A novel deep learning approach for wind power forecasting based on wd-lstm model,” *Energies*, vol. 13, no. 18, p. 4964, 2020.
- [26] H. Quan, A. Khosravi, D. Yang, and D. Srinivasan, “A survey of computational intelligence techniques for wind power uncertainty quantification in smart grids,” *IEEE transactions on neural*



- networks and learning systems*, vol. 31, no. 11, pp. 4582–4599, 2019.
- [27] A. Khosravi and S. Nahavandi, “An optimized mean variance estimation method for uncertainty quantification of wind power forecasts,” *International Journal of Electrical Power & Energy Systems*, vol. 61, pp. 446–454, 2014.
- [28] R. Ak, V. Vitelli, and E. Zio, “An interval-valued neural network approach for uncertainty quantification in short-term wind speed prediction,” *IEEE transactions on neural networks and learning systems*, vol. 26, no. 11, pp. 2787–2800, 2015.
- [29] M. C. Kennedy and A. O’Hagan, “Predicting the output from a complex computer code when fast approximations are available,” *Biometrika*, vol. 87, no. 1, pp. 1–13, 2000.
- [30] A. G. Hawkes and D. Oakes, “A cluster process representation of a self-exciting process,” *Journal of Applied Probability*, pp. 493–503, 1974.
- [31] P. A. Hwang and D. W. Wang, “Do wind-generated waves under steady forcing propagate primarily in the downwind direction?” *arXiv preprint arXiv:1907.01532*, 2019.
- [32] C. E. Rasmussen, “Gaussian processes in machine learning,” in *Summer school on machine learning*. Springer, 2003, pp. 63–71.
- [33] M. Titsias, “Variational learning of inducing variables in sparse gaussian processes,” in *Artificial intelligence and statistics*. PMLR, 2009, pp. 567–574.
- [34] J. Hensman, N. Fusi, and N. D. Lawrence, “Gaussian processes for big data,” *arXiv preprint arXiv:1309.6835*, 2013.
- [35] J. Hensman, A. Matthews, and Z. Ghahramani, “Scalable variational gaussian process classification,” in *Artificial Intelligence and Statistics*. PMLR, 2015, pp. 351–360.
- [36] S. Zhu, A. Bukharin, L. Xie, S. Yang, P. Keskinocak, and Y. Xie, “Early detection of covid-19 hotspots using spatio-temporal data,” *arXiv preprint arXiv:2106.00072*, 2021.
- [37] E. Snelson and Z. Ghahramani, “Sparse gaussian processes using pseudo-inputs,” *Advances in neural information processing systems*, vol. 18, pp. 1257–1264, 2005.
- [38] M. D. Hoffman and M. J. Johnson, “Elbo surgery: yet another way to carve up the variational evidence lower bound,” in *Workshop in Advances in Approximate Bayesian Inference, NIPS*, vol. 1, no. 2, 2016.
- [39] S. Kullback and R. A. Leibler, “On information and sufficiency,” *The annals of mathematical statistics*, vol. 22, no. 1, pp. 79–86, 1951.
- [40] Q. Liu and D. A. Pierce, “A note on gauss—hermite quadrature,” *Biometrika*, vol. 81, no. 3, pp. 624–629, 1994.
- [41] V. A. Traag, L. Waltman, and N. J. Van Eck, “From louvain to leiden: guaranteeing well-connected communities,” *Scientific reports*, vol. 9, no. 1, pp. 1–12, 2019.
- [42] J. Martens, “New insights and perspectives on the natural gradient method,” *arXiv preprint arXiv:1412.1193*, 2014.
- [43] J. Catalão, H. Pousinho, and V. Mendes, “Short-term wind power forecasting in portugal by neural networks and wavelet transform,” *Renewable Energy*, vol. 36, no. 4, pp. 1245–1251, 2011. [Online]. Available: <https://www.sciencedirect.com/science/article/pii/S0960148110004477>

APPENDIX A  
EXTRACTING DDG

---

**Algorithm 1:** Algorithm for extracting DDG.

---

**Input:** wind direction:  $\{\omega_{jt}^{k,\eta}\} \in [0, 2\pi)^{k \times (T/\eta)}$ ;  
cardinal direction from cluster  $j$  to  $i$ :  $\varphi_{ji}^k$ ; graph  
support:  $\mathcal{G}^k$ ;  
**Initialization:**  $\mathcal{G}^{k,\eta} = \{\mathcal{V}^k, \{\mathcal{E}_t^k = \emptyset\}_{t \in \mathcal{T}^\eta}\}$ ;  
**for**  $t \in \mathcal{T}^\eta$  **do**  
    **for**  $(j, i) \in \mathcal{G}^k \subseteq \mathcal{V}^{k^2}$  **do**  
        **if**  $|\varphi_{ji}^k - \omega_{jt}^{k,\eta}| \leq \pi/12$  **then**  
             $\mathcal{E}_t^k \leftarrow \mathcal{E}_t^k \cup (j, i)$ ;  
        **end**  
    **end**  
**end**

---

APPENDIX B  
DERIVATION OF ELBO

Assume the posterior distribution  $p(\boldsymbol{\epsilon}, \mathbf{u}|\mathbf{y})$  over random variable vector  $\boldsymbol{\epsilon}$  and  $\mathbf{u}$  is approximated by a variational distribution  $q(\boldsymbol{\epsilon}, \mathbf{u})$ . Suppose this variational distribution  $q(\boldsymbol{\epsilon}, \mathbf{u})$  can be factorized as  $q(\boldsymbol{\epsilon}, \mathbf{u}) = p(\boldsymbol{\epsilon}|\mathbf{u})q(\mathbf{u})$ . Hence, the ELBO can be derived as follows:

$$\begin{aligned}
\log p(\mathbf{y}) &= \log \int \int p(\mathbf{y}|\boldsymbol{\epsilon}, \mathbf{u})p(\boldsymbol{\epsilon}, \mathbf{u})d\boldsymbol{\epsilon}d\mathbf{u} \\
&= \log \int \int p(\mathbf{y}|\boldsymbol{\epsilon})p(\boldsymbol{\epsilon}, \mathbf{u})d\boldsymbol{\epsilon}d\mathbf{u} \\
&= \log \int \int p(\mathbf{y}|\boldsymbol{\epsilon})p(\boldsymbol{\epsilon}, \mathbf{u})\frac{q(\boldsymbol{\epsilon}, \mathbf{u})}{q(\boldsymbol{\epsilon}, \mathbf{u})}d\boldsymbol{\epsilon}d\mathbf{u} \\
&= \log \mathbb{E}_{q(\boldsymbol{\epsilon}, \mathbf{u})} \left[ p(\mathbf{y}|\boldsymbol{\epsilon})\frac{p(\boldsymbol{\epsilon}, \mathbf{u})}{q(\boldsymbol{\epsilon}, \mathbf{u})} \right] \\
&\stackrel{(i)}{\geq} \mathbb{E}_{q(\boldsymbol{\epsilon}, \mathbf{u})} \log \left[ p(\mathbf{y}|\boldsymbol{\epsilon})\frac{p(\boldsymbol{\epsilon}, \mathbf{u})}{q(\boldsymbol{\epsilon}, \mathbf{u})} \right] \\
&= \int \int \log p(\mathbf{y}|\boldsymbol{\epsilon})q(\boldsymbol{\epsilon}, \mathbf{u})d\boldsymbol{\epsilon}d\mathbf{u} - \\
&\quad \int \int \log \left( \frac{q(\boldsymbol{\epsilon}, \mathbf{u})}{p(\boldsymbol{\epsilon}, \mathbf{u})} \right) q(\boldsymbol{\epsilon}, \mathbf{u})d\boldsymbol{\epsilon}d\mathbf{u} \\
&\stackrel{(ii)}{=} \mathbb{E}_{q(\boldsymbol{\epsilon})} [\log p(\mathbf{y}|\boldsymbol{\epsilon})] - \text{KL} [q(\mathbf{u})||p(\mathbf{u})],
\end{aligned}$$

where  $q(\boldsymbol{\epsilon})$  is the marginal of  $\boldsymbol{\epsilon}$  from the joint variational distribution  $q(\boldsymbol{\epsilon}, \mathbf{u})$ , by integrating  $\mathbf{u}$  out. The inequality (i) holds due to the the Jensen's inequality. The equality (ii) holds because

$$\begin{aligned}
&\int \int \log \left( \frac{q(\boldsymbol{\epsilon}, \mathbf{u})}{p(\boldsymbol{\epsilon}, \mathbf{u})} \right) q(\boldsymbol{\epsilon}, \mathbf{u})d\boldsymbol{\epsilon}d\mathbf{u} \\
&= \int \int \log \left( \frac{p(\boldsymbol{\epsilon}|\mathbf{u})q(\mathbf{u})}{p(\boldsymbol{\epsilon}|\mathbf{u})p(\mathbf{u})} \right) q(\boldsymbol{\epsilon}, \mathbf{u})d\boldsymbol{\epsilon}d\mathbf{u} \\
&= \int \int \log \left( \frac{q(\mathbf{u})}{p(\mathbf{u})} \right) q(\boldsymbol{\epsilon}, \mathbf{u})d\boldsymbol{\epsilon}d\mathbf{u}
\end{aligned}$$

$$\begin{aligned}
&= \int \log \left( \frac{q(\mathbf{u})}{p(\mathbf{u})} \right) \left( \int q(\boldsymbol{\epsilon}, \mathbf{u})d\boldsymbol{\epsilon} \right) d\mathbf{u} \\
&= \int \log \left( \frac{q(\mathbf{u})}{p(\mathbf{u})} \right) q(\mathbf{u})d\mathbf{u} \\
&= \text{KL} [q(\mathbf{u})||p(\mathbf{u})].
\end{aligned}$$

To calculate the ELBO, we also need to derive the analytical expression for  $q(\boldsymbol{\epsilon})$  and  $\text{KL}[q(\mathbf{u})||p(\boldsymbol{\epsilon})]$ . First, given the joint distribution defined in (6), we apply the multivariate Guassian conditional rule and have the closed-form expression for the conditional distribution:

$$p(\boldsymbol{\epsilon}|\mathbf{u}) = \mathcal{N}(\boldsymbol{\epsilon}|\mathbf{A}\mathbf{u}, \mathbf{B}),$$

where  $\mathbf{A} = \mathbf{K}_{XZ}\mathbf{K}_{ZZ}^{-1}$  and  $\mathbf{B} = \mathbf{K}_{XX} - \mathbf{K}_{XZ}\mathbf{K}_{ZZ}^{-1}\mathbf{K}_{XZ}^\top$ . Now, due to the factorization  $q(\boldsymbol{\epsilon}, \mathbf{u}) = p(\boldsymbol{\epsilon}|\mathbf{u})q(\mathbf{u})$ , we have

$$\begin{aligned}
q(\boldsymbol{\epsilon}) &= \int q(\boldsymbol{\epsilon}, \mathbf{u})d\mathbf{u} \\
&= \int p(\boldsymbol{\epsilon}|\mathbf{u})q(\mathbf{u})d\mathbf{u} \\
&= \int \mathcal{N}(\boldsymbol{\epsilon}|\mathbf{A}\mathbf{u}, \mathbf{B}) \cdot \mathcal{N}(\mathbf{u}|\mathbf{m}, \mathbf{S})d\mathbf{u} \\
&= \int \mathcal{N}(\boldsymbol{\epsilon}|\mathbf{A}\mathbf{m}, \mathbf{A}\mathbf{S}\mathbf{A}^\top + \mathbf{B}) \cdot \mathcal{N}(\mathbf{u}|\mathbf{m}, \mathbf{S})d\mathbf{u} \\
&= \mathcal{N}(\boldsymbol{\epsilon}|\mathbf{A}\mathbf{m}, \mathbf{A}\mathbf{S}\mathbf{A}^\top + \mathbf{B}) \cdot \int \mathcal{N}(\mathbf{u}|\mathbf{m}, \mathbf{S})d\mathbf{u} \\
&= \mathcal{N}(\boldsymbol{\epsilon}|\mathbf{A}\mathbf{m}, \mathbf{K}_{XX} + \mathbf{A}(\mathbf{S} - \mathbf{K}_{ZZ})\mathbf{A}^\top).
\end{aligned}$$

Next, we derive the analytical expression for the KL divergence in the ELBO, since both  $q(\mathbf{u}) = \mathcal{N}(\mathbf{u}|\mathbf{m}, \mathbf{S})$  and  $p(\mathbf{u}) = \mathcal{N}(\mathbf{u}|\mathbf{0}, \mathbf{K}_{ZZ})$  are multivariate Gaussian distributions. Therefore, the KL divergence between  $q(\mathbf{u})$  and  $p(\mathbf{u})$  is:

$$\begin{aligned}
\text{KL} [q(\mathbf{u})||p(\mathbf{u})] &= \frac{1}{2} \left( \log \left( \frac{\det(\mathbf{K}_{ZZ})}{\det(\mathbf{S})} \right) - M + \right. \\
&\quad \left. \text{tr}(\mathbf{K}_{ZZ}^{-1}\mathbf{S}) + (\mathbf{0} - \mathbf{m})^\top \mathbf{K}_{ZZ}^{-1}(\mathbf{0} - \mathbf{m}) \right),
\end{aligned}$$

where  $\det(\cdot)$  is the matrix determinant and  $\text{tr}(\cdot)$  is the trace of matrix.

APPENDIX C  
STOCHASTIC GRADIENT BASED OPTIMIZATION

In this section, we describe our learning algorithm. The optimal parameters of the proposed multi-resolution model can be found by maximizing (5) using gradient-based optimization. However, the full gradient evaluation can still be expensive to be carried out. With a sparse prior (inducing variables), even though we can tackle the computational challenge in inverting a big matrix, evaluating the gradient of the first term in (8) still requires the full data set, which is memory-intensive if the size of the data set  $N$  is too large. To alleviate the problem

of expensive gradient evaluation, we adopt a stochastic gradient based method [34] and only compute the gradient of the objective function evaluated on a random subset of the data at each iteration.

Specifically, to apply stochastic gradient descent to the variational parameters  $(\mathbf{Z}, \mathbf{m}, \mathbf{S})$  in our GP model, we follow the idea of [34], [42] by taking steps in the direction of the approximate natural gradient, which is given by the usual gradient re-scaled by the inverse Fisher information. The learning algorithm has been summarized in Algorithm 2.

---

**Algorithm 2:** Learning algorithm for the proposed model

---

**Initialization:** Randomly initialize  $\theta, \mathbf{Z}, \mathbf{m}, \mathbf{S}$ ;  
**Input:** Data set  $\mathbf{X}, \mathbf{y}, \mathbf{h}$ ; Number of iterations  $B$ ; Batch size  $n$ ;  
**for**  $b = \{1, \dots, B\}$  **do**  
  Sample a subset  $\mathbf{X}_b, \mathbf{y}_b, \mathbf{h}_b$  with  $n$  points from  $\mathbf{X}, \mathbf{y}, \mathbf{h}$ , respectively;  
  Calculate ELBO of  $\ell_h$  and  $\ell_y$  based on (8) given data  $\mathbf{X}_b, \mathbf{y}_b, \mathbf{h}_b$ ;  
  Calculate the gradient of (5) *w.r.t.*  $\theta$ ;  
  Calculate the natural gradient of (5) *w.r.t.*  $\mathbf{Z}, \mathbf{m}, \mathbf{S}$ ;  
  Ascend the gradient of  $\theta, \mathbf{Z}, \mathbf{m}, \mathbf{S}$ ;  
**end**

---

#### APPENDIX D

##### DERIVATION OF PREDICTIVE POSTERIOR

A Bayesian model makes predictions based on the posterior distribution. Given testing locations  $\mathbf{X}_*$ , we can derive the predictive posterior distribution  $p(\boldsymbol{\epsilon}_* | \mathbf{y}, \mathbf{h})$ :

$$\begin{aligned}
p(\boldsymbol{\epsilon}_* | \mathbf{y}) &= \int \int p(\boldsymbol{\epsilon}_*, \boldsymbol{\epsilon}, \mathbf{u} | \mathbf{y}, \mathbf{h}) d\boldsymbol{\epsilon} d\mathbf{u} \\
&= \int \int p(\boldsymbol{\epsilon}_* | \boldsymbol{\epsilon}, \mathbf{u}, \mathbf{y}, \mathbf{h}) d\boldsymbol{\epsilon} d\mathbf{u} \\
&= \int \int p(\boldsymbol{\epsilon}_* | \boldsymbol{\epsilon}, \mathbf{u}, \mathbf{y}, \mathbf{h}) p(\boldsymbol{\epsilon}, \mathbf{u} | \mathbf{y}, \mathbf{h}) d\boldsymbol{\epsilon} d\mathbf{u} \\
&= \int \int p(\boldsymbol{\epsilon}_* | \boldsymbol{\epsilon}, \mathbf{u}) p(\boldsymbol{\epsilon}, \mathbf{u} | \mathbf{y}, \mathbf{h}) d\boldsymbol{\epsilon} d\mathbf{u} \\
&= \int \int p(\boldsymbol{\epsilon}_* | \boldsymbol{\epsilon}, \mathbf{u}) q(\boldsymbol{\epsilon}, \mathbf{u}) d\boldsymbol{\epsilon} d\mathbf{u} \\
&= \int \int p(\boldsymbol{\epsilon}_* | \boldsymbol{\epsilon}, \mathbf{u}) p(\boldsymbol{\epsilon} | \mathbf{u}) q(\mathbf{u}) d\boldsymbol{\epsilon} d\mathbf{u} \\
&= \int \left( \int p(\boldsymbol{\epsilon}_* | \boldsymbol{\epsilon}, \mathbf{u}) p(\boldsymbol{\epsilon} | \mathbf{u}) d\boldsymbol{\epsilon} \right) q(\mathbf{u}) d\mathbf{u} \\
&= \int \left( \int p(\boldsymbol{\epsilon}_*, \boldsymbol{\epsilon} | \mathbf{u}) d\boldsymbol{\epsilon} \right) q(\mathbf{u}) d\mathbf{u} \\
&= \int p(\boldsymbol{\epsilon}_* | \mathbf{u}) q(\mathbf{u}) d\mathbf{u}
\end{aligned}$$

$$\begin{aligned}
&= p(\boldsymbol{\epsilon}_* | \mathbf{u}) \int q(\mathbf{u}) d\mathbf{u} \\
&= p(\boldsymbol{\epsilon}_* | \mathbf{u}).
\end{aligned}$$

Similar to (6), since we assume that the unobserved future data comes from the same generation process, i.e.,

$$p(\boldsymbol{\epsilon}_*, \mathbf{u}) = \mathcal{N} \left( \begin{bmatrix} \boldsymbol{\epsilon}_* \\ \mathbf{u} \end{bmatrix} \middle| \mathbf{0}, \begin{bmatrix} \mathbf{K}_{**} & \mathbf{K}_{*Z} \\ \mathbf{K}_{*Z}^\top & \mathbf{K}_{*Z} \end{bmatrix} \right),$$

we can apply the multivariate Gaussian conditional rule on the prior  $p(\boldsymbol{\epsilon}_*, \mathbf{u})$  and obtain:

$$\begin{aligned}
p(\boldsymbol{\epsilon}_* | \mathbf{u}) &= \mathcal{N}(\boldsymbol{\epsilon}_* | \mathbf{A}_* \mathbf{u}, \mathbf{B}_*) \\
&= \mathcal{N}(\boldsymbol{\epsilon}_* | \mathbf{A}_* \mathbf{m}, \mathbf{A}_* \mathbf{S} \mathbf{A}_*^\top + \mathbf{B}_*)
\end{aligned}$$

where  $\mathbf{A}_* = \mathbf{K}_{*Z} \mathbf{K}_{ZZ}^{-1}$  and  $\mathbf{B}_* = \mathbf{K}_{**} - \mathbf{K}_{*Z} \mathbf{K}_{ZZ}^{-1} \mathbf{K}_{*Z}^\top$ .

#### APPENDIX E

##### DETAILED DESCRIPTION FOR THE BASELINE METHODS

The detailed description of baseline models and the choices of parameters presented in Table II is as follows:

We compare a neural network-based univariate prediction model (NN) on our dataset following the framework proposed by [43]. The neural network contains three layers, where the width of each hidden layer is six and Hyperbolic function is adopted as its activation layer. We first slice the data of previous 12 hours and feed them into the network as four features, where each feature contains 3 hours of data, then predict the next 3 hours using the output of the network.

We consider a vector autoregressive (VAR) model, which is a generalization of the autoregressive model and extends the univariate time series to the multivariate scenarios. Let the true wind average wind speed under data resolution  $(\kappa, \eta)$  at time  $t$  be  $y^{\kappa, \eta}(t)$ . VAR( $p$ ) model can be defined as

$$y^{\kappa, \eta}(t) = c + \sum_{\tau=1}^p A_\tau y^{\kappa, \eta}(t - \tau) + \boldsymbol{\epsilon}_t, \quad (10)$$

Where  $c$  is the intercept vector of size  $\kappa$ ,  $p$  is the time lag,  $A_\tau$  is coefficient matrix of size  $\kappa \times \kappa$ , and  $\boldsymbol{\epsilon}_t$  is the  $\kappa$ -dimensional error term. Here, we set  $p = 10$ .

We also compare Long Short-Term Memory (LSTM), which is a recurrent neural network architecture that has been widely used to model temporal data. We apply a sliding window of size  $d$  on the raw data, which converts the input of LSTM to matrices of size  $\kappa \times d$  and the output of LSTM to vectors of size  $\kappa \times 1$ . The input vector is passed into a LSTM unit of hidden size eight. The output of LSTM is later passed into a dense layer to reduce the output dimension to 1.

APPENDIX F  
ADDITIONAL EXPERIMENTAL RESULTS

This section presents additional experimental results in this study. We first present an illustration of our one-step ahead prediction in Fig. 11. We note that the out-of-sample prediction results in Fig. 7 and Fig. 8 are carried out at more than 280 time units (1 hour per unit). In Fig. 12, we show four examples of the prediction error of the STDR at different data resolutions. We also show the fitted matrices  $\{\alpha_{ji}^{\kappa,\eta}\}$  for data resolution  $\eta = 4$  and  $\kappa \in \{20, 30, 40, 50\}$  in Fig. 13 and their corresponding detected communities using Leiden algorithm [41] in Fig. 14.

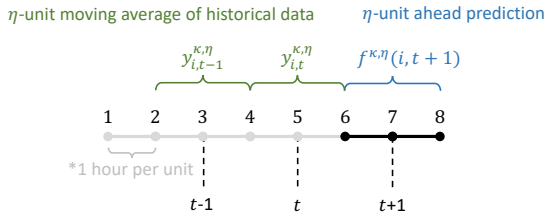


Fig. 11: An illustration of one-step ahead or  $\eta$ -unit ahead prediction. The out-of-sample predictions can be carried out on each time unit (1 hour per unit). In this example,  $\eta = 2$ .

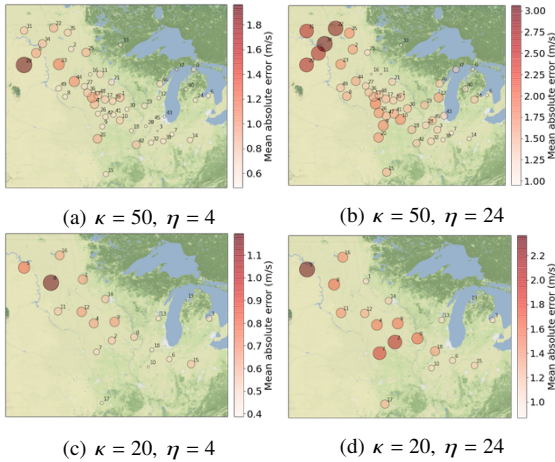


Fig. 12: Mean absolute error (MAE) of spatio-temporal wind speed predictions suggested by STDR at four different data resolutions. The ID of each cluster is shown on the map. The size and color of each dot represent the MAE of the corresponding cluster.

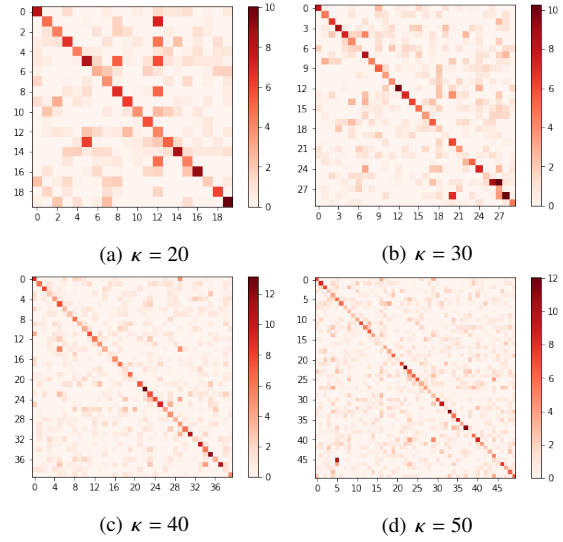


Fig. 13: Fitted  $\{\alpha_{ji}^{\kappa,\eta}\}$  ( $\eta = 4$ ) for different  $\kappa$ . The horizontal and vertical coordinates represent the cluster's ID. The color depth of each cell represents the  $\alpha_{ji}^{\kappa,\eta}$  value of the corresponding edge  $(j, i)$ .

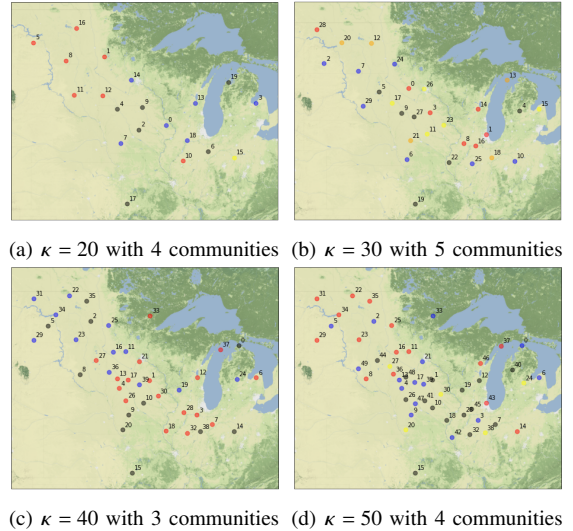


Fig. 14: Detected communities in fitted  $\{\alpha_{ji}^{\kappa,\eta}\}$  ( $\eta = 4$ ) using Leiden algorithm for different  $\kappa$ . The ID of each cluster is shown on the map. The set of clusters with the same color are identified as a “community”.